An investigation of SGS stress anisotropy modeling in complex turbulent flow fields

ABE, Ken-ichi
Department of Aeronautics and Astronautics, Faculty of Engineering, Kyushu University : Professor

出版情報：Flow, Turbulence and Combustion. 92 (1/2), pp.503-525, 2013-10-31. Springer Nature
バージョン：
権利関係：

Flow, Turbulence and Combustion manuscript No.
(will be inserted by the editor)

An investigation of SGS stress anisotropy modeling in complex turbulent flow fields

Ken-ichi ABE

Received: date / Accepted: date

Abstract An anisotropy-resolving subgrid-scale (SGS) model for large eddy simulation was investigated. Primary attention was given to the predictive performance of the SGS model in the case of complex turbulence with flow impingement and/or flow separation. The SGS model was constructed by combining an isotropic linear eddy-viscosity model with an extra anisotropic term. Since the extra anisotropic term was modeled to prevent undesirable energy transfer between the grid-scale and SGS parts, the model is expected not to seriously affect computational stability. To validate the model performance for complex turbulent flow fields, the SGS model was applied to numerical simulations of a plane impinging jet and 3-D diffuser flow as well as fundamental plane channel flows. The SGS model provided reasonable predictions for these test cases. Furthermore, the predicted SGS stress components were decomposed into linear and anisotropic parts and their roles were investigated in detail. The usefulness of the present anisotropy-resolving SGS model in practical engineering applications was thus described.

Keywords Large-eddy simulation · SGS stress anisotropy · Scale-similarity model · Plane impinging jet · 3-D diffuser flow

Ken-ichi ABE
Professor, Department of Aeronautics and Astronautics, Kyushu University, Fukuoka 819-0395, Japan
Tel.: +81-92-8023023
Fax: +81-92-8023001
E-mail: abe@aero.kyushu-u.ac.jp

Nomenclature

b_{ij}	anisotropy tensor
C_f	friction coefficient
C_p	pressure coefficient
D	inlet channel width of plane impinging jet
H, W	inlet rectangular-duct height and width of 3D-diffuser flow, respectively
k_{SGS}	SGS turbulence energy
$\overline{P}$	filtered static pressure
Q	second invariant of velocity-fluctuation gradient tensor, $\left(\partial u_i^{'}/\partial x_j\right)\left(\partial u_j^{'}/\partial x_i\right)$
R_{ij}^{*}	SGS stress anisotropy expression
Re_τ	Reynolds number based on friction velocity and half channel height
S_{ij}	strain-rate tensor, $\left(\partial\overline{U}_i/\partial x_j + \partial\overline{U}_j/\partial x_i\right)/2$
t	time
$\overline{U}, \overline{V}$	filtered velocity in x- and y-directions, respectively
$\overline{U}_i$	filtered velocity in i-direction
U_b	inlet bulk-mean velocity
u_τ	friction velocity
x, y, z	Cartesian coordinates
x_i	Cartesian coordinate in i-direction
δ	half channel height
Δ	SGS filter width
$\Delta x, \Delta y, \Delta z$	grid widths in x-, y- and z-directions, respectively
ε_{SGS}	dissipation rate of SGS turbulence energy
ν, ν_{SGS}	kinematic and SGS eddy viscosities, respectively
ρ	density
τ_{ij}	SGS stress tensor

Special symbols

$(\ )^+$	value normalized by friction velocity
$\overline{(\ )}$	filtered value
$\widehat{(\ )}$	test-filtered value
$\langle(\ )\rangle$	ensemble-averaged value
$(\ )^{'}$	fluctuation from ensemble-averaged value
$(\ )_{rms}^{'}$	root-mean square value of fluctuation, $\sqrt{\langle(\ )^{'2}\rangle}$

1 Introduction

Large eddy simulation (LES) is well known as a useful tool for predicting complex turbulence in engineering applications. In LES, grid-scale (GS) eddies are directly resolved and subgrid-scale (SGS) eddies must be modeled. The governing equations for incompressible turbulence may be written as

$$\frac{\partial \overline{U}_i}{\partial x_i} = 0,$$

$$\frac{\mathrm{D}\overline{U}_i}{\mathrm{D}t} = -\frac{1}{\rho}\frac{\partial \overline{P}}{\partial x_i} + \frac{\partial}{\partial x_j}\left\{\nu\left(\frac{\partial \overline{U}_i}{\partial x_j} + \frac{\partial \overline{U}_j}{\partial x_i}\right) - \tau_{ij}\right\}, \tag{1}$$

where $\overline{(\ )}$ denotes a filtered value. In Eq. (1), ρ, $\overline{P}$, $\overline{U}_i$ and ν denote the density, filtered static pressure, filtered velocity and kinematic viscosity, respectively. The SGS stress tensor τ_{ij} is originally expressed as $\tau_{ij} = \overline{U_i U_j} - \overline{U}_i \overline{U}_j$.

For τ_{ij}, a linear eddy-viscosity model (EVM) is most often used. The canonical form is

$$\tau_{ij}{}^a = -2\nu_{SGS} S_{ij}, \quad S_{ij} = \frac{1}{2}\left(\frac{\partial \overline{U}_i}{\partial x_j} + \frac{\partial \overline{U}_j}{\partial x_i}\right), \tag{2}$$

where S_{ij} denotes the strain-rate tensor and $\tau_{ij}{}^a = \tau_{ij} - \tau_{kk}\delta_{ij}/3$. The Smagorinsky model[1] is a representative EVM. Although an EVM is easily introduced into existing CFD code, its principal direction does not align with that of the real SGS stress. The SGS stress is not a scalar, but rather a tensor that includes not only the SGS shear stress, but also the SGS normal stresses. Therefore, the final goal of SGS stress modeling is essentially to reproduce all the SGS stress components properly. Their correct reproduction is directly related to the correct prediction of the alignment of the principal axis.

To improve the predictive performance of the conventional Smagorinsky model, the development of a dynamic Smagorinsky model may be promising (see for example, Germano et al.[2] and Lilly[3]). In this model, the model coefficient of ν_{SGS} is locally determined by means of a dynamic procedure. The dynamic Smagorinsky model potentially provides both the forward scatter and the back scatter, although a linear EVM expression is adopted. However, this type of SGS model is also known to cause numerical instability owing to an excessive effect of the back scatter, in particular for coarse-grid resolution. To avoid such numerical instability, we often restrict the back scatter by clipping negative values of ν_{SGS}. This makes the computation stable but very dissipative, and the predictive performance thus reduces as the grid resolution becomes coarser.

An alternative method to improve the prediction accuracy is the so-called "scale-similarity model", the most popular version of which is the model proposed by Bardina et al.[4]. Their SGS Reynolds-stress model is expressed as

$$\tau_{ij} = C_B\left(\overline{U}_i - \widehat{\overline{U}}_i\right)\left(\overline{U}_j - \widehat{\overline{U}}_j\right), \tag{3}$$

where $\widehat{(\ )}$ denotes a test-filtering operator. This type of model is known to provide much better alignment with the real SGS stress tensor (see for example, Horiuti[5]). However, it is not always dissipative and it often suffers from numerical instability. This defect originates from the fact that the model often provides negative energy

transfer (i.e., back scatter), as is also seen in LES with the dynamic Smagorinsky model.

Thus far, many research groups have tackled this crucial problem, and among solutions to the problem, the concept of a "mixed model" is worth noting. The mixed model is a combination of the scale-similarity model and a dissipative EVM such as the Smagorinsky model (see for example, references [6]–[10]). Note that to improve model performance, some mixed models introduce a dynamic procedure to determine model coefficients. For instance, Sarghini et al.[9] investigated the performance of several mixed SGS models for fundamental channel flows and a three-dimensional boundary-layer flow. Although they found model performance to be generally acceptable, several issues remain in the application of mixed SGS models to high-Re turbulence with coarse-grid resolution. On the other hand, Morinishi and Vasilyev[10] proposed an improved dynamic procedure to determine the coefficients of a mixed SGS model. Their resulting SGS model provided encouraging results for channel-flow cases with various grid resolutions, while the computational stability is still unknown when applying the model to complex turbulence with flow impingement and/or flow separation. Therefore, there remains an important issue relating to computational stability, although the mixed models and their extensions have provided encouraging results. In such simulation, the numerical instability introduced by the scale-similarity model is thought to be much stronger than the dissipative feature of the EVM adopted in a mixed model. Obviously, this is an undesirable feature for further application of an SGS model to high-Re complex turbulence.

Considering the above discussion, an idea emerges that we may successfully reproduce all the SGS stress components with stable computation, if we can successfully exclude the factor causing numerical instability from a scale-similarity model. Such a modeling strategy is expected to contribute considerably to the engineering field. For this purpose, Abe[11] recently proposed a new anisotropy-resolving SGS modeling concept, where the SGS stress expression was constructed by combining an isotropic EVM with an extra anisotropic term newly proposed. The primary concern with this SGS model was how to maintain computational stability, while improving predictive accuracy, particularly for a coarse grid resolution in the near-wall region. Applications of the model to channel flows with various grid resolutions illustrated the basic capability of this SGS modeling concept.

Although the performance of this anisotropy-resolving SGS model was generally acceptable for application to a fundamental plane channel flow, there remain points to be further investigated. First, it needs to be clarified how the model represents the SGS stress anisotropy. Second, an important concern is the model performance for more complex turbulence with flow impingement and/or flow separation. Therefore, in this study, to investigate the aforementioned issues in detail, the anisotropy-resolving SGS model proposed by Abe[11] is applied to numerical simulations of a plane impinging jet and a three-dimensional (3-D) diffuser flow as well as fundamental plane channel flows. In the channel-flow case, the obtained SGS stress components are decomposed into linear (almost isotropic) and extra anisotropic parts and compared with each other. In the cases of the plane impinging jet and the 3-D diffuser flow, the computational results are compared with those of the direct numerical simulation (DNS) and corresponding experimental data, respectively.

2 Turbulence Model

In this section, we briefly describe the anisotropy-resolving SGS model proposed by Abe[11]. We start with the representative scale-similarity model[4]:

$$\tau_{ij}^* = C_B \left(\overline{U}_i - \widehat{\overline{U}}_i \right) \left(\overline{U}_j - \widehat{\overline{U}}_j \right). \tag{4}$$

Note that, for convenience in the following discussion, another temporary notation τ_{ij}^* is used here for the SGS stress tensor (although this is basically the same as Eq. (3)). In this study, to calculate a test-filtered value $\widehat{\overline{U}}_i$, we adopted a box-type (volume-averaging-type) filtering operator.

Next, we consider an EVM-type linear approximation for Eq. (4) with an equivalent eddy viscosity ν^* :

$$\tau_{ij}^{*\,a} S_{ij} = -2\nu^* S_{ij} S_{ij} = -2\nu^* S^2 \qquad \longrightarrow \qquad \nu^* = -\frac{\tau_{ij}^{*\,a} S_{ij}}{2S^2}\ , \tag{5}$$

where $S^2 = S_{ij} S_{ij}$ and $\tau_{ij}^{*\,a} = \tau_{ij}^* - \tau_{kk}^* \delta_{ij}/3$. Considering that the production term of the SGS turbulence energy k_{SGS} is expressed as $-\tau_{ij}^* \partial \overline{U}_i / \partial x_j$ $(= -\tau_{ij}^* S_{ij})$, Eq. (5) indicates that this linearized approximation yields the same amount of energy transfer between the GS and SGS components as the original scale-similarity model. Since the linear EVM $(-2\nu^* S_{ij})$ is recognized as an isotropic approximation of the original model $(\tau_{ij}^{*\,a})$, it may be useful to represent the SGS stress anisotropy with the residual expression

$$R_{ij}^* = \tau_{ij}^{*\,a} - \left(-2\nu^* S_{ij} \right), \tag{6}$$

where R_{ij}^* is an "SGS stress anisotropy term" that is evaluated by subtracting an EVM form from the original Bardina model. It is found from Eq. (5) that R_{ij}^* yields no undesirable extra energy transfer between the GS and SGS components. Therefore, Eq. (6) is expected to successfully predict the SGS stress anisotropy without seriously affecting the computational stability.

On the basis of the above discussion, Abe[11] proposed an SGS model for τ_{ij} in Eq. (1), which is constructed by combining a representative isotropic EVM with an extra anisotropic term:

$$\tau_{ij} = \frac{2}{3}\ k_{SGS}\ \delta_{ij} - 2\ \nu_{SGS}\ S_{ij} + 2\ k_{SGS}\ b_{ij}^{SGS}. \tag{7}$$

In Eq. (7), the anisotropy tensor b_{ij}^{SGS} is modeled as

$$b_{ij}^{SGS} = \frac{\tau_{ij}^* - (-2\nu^* S_{ij})}{\tau_{kk}^* - (-2\nu^* S_{kk})} - \frac{1}{3}\delta_{ij} = \frac{\tau_{ij}^* - \tau_{kk}^* \delta_{ij}/3 - (-2\nu^* S_{ij})}{\tau_{kk}^*} = \frac{R_{ij}^*}{\tau_{kk}^*}\ , \tag{8}$$

where τ_{ij}^* is given by Eq. (4). It should be noted that the simulation results by the present SGS model never depend on the model constant C_B. Although C_B is included in the third term on the right-hand side of Eq. (7), it appears in both numerator (R_{ij}^*) and denominator (τ_{kk}^*) of b_{ij}^{SGS} in the same way. Therefore, C_B is completely canceled and thus no effect appears in the simulation results, as long as k_{SGS} is separately determined using its transport equation such as the present one-equation SGS model. As seen in Eq. (8), the present anisotropy tensor

b_{ij}^{SGS} takes into account the basic concept discussed for Eq. (6) and is expected to reflect its fundamental features. Although the form of Eq. (7) may appear odd, this type of modeling strategy that introduces the anisotropy-tensor form is often adopted in the field of non-linear eddy-viscosity Reynolds-averaged Navier-Stokes (RANS) modeling (see for example, Gatski and Speziale[12]; Craft et al.[13]; Abe et al.[14]). This form is expected to successfully guarantees the realizability of the stress anisotropy.

On the other hand, for the linear EVM in Eq. (7), the present SGS model introduces the one-equation SGS model proposed by Inagaki[15]. The SGS viscosity ν_{SGS} is modeled as

$$\nu_{SGS} = C_{SGS}\ f_{SGS}\sqrt{k_{SGS}}\ \Delta, \qquad f_{SGS} = 1 - \exp\left\{-\left(\frac{y_\varepsilon^*}{A_0}\right)^{4/3}\right\}, \tag{9}$$

where $C_{SGS}(= 0.05)$ and $A_0(= 30)$ are the model constants. In the model function f_{SGS}, the wall-distance parameter y_ε^* is modeled as[15]:

$$y_\varepsilon^* = \left(\frac{u_\varepsilon y}{\nu}\right)\sqrt{C_l\frac{y}{\Delta}}, \qquad u_\varepsilon = (\nu\varepsilon_{SGS})^{1/4}, \tag{10}$$

where $C_l(= 4)$ is the model constant. In this study, ε_{SGS} is algebraically evaluated using the expression

$$\varepsilon_{SGS} = C_\varepsilon\ \frac{{k_{SGS}}^{3/2}}{\Delta} + \frac{2\nu k_{SGS}}{y^2}\ , \tag{11}$$

where $C_\varepsilon(= 0.835)$ is the model constant. Note that the second term on the right-hand side of Eq. (11) is introduced to guarantee the correct near-wall limiting behavior of ε_{SGS}. On the other hand, k_{SGS} is determined from the transport equation

$$\frac{\mathrm{D}k_{SGS}}{\mathrm{D}t} = \frac{\partial}{\partial x_j}\left\{\left(\nu + \frac{\nu_{SGS}}{\sigma_k}\right)\frac{\partial k_{SGS}}{\partial x_j}\right\} - \tau_{ij}\frac{\partial \overline{U}_i}{\partial x_j} - \varepsilon_{SGS}\ , \tag{12}$$

where $\sigma_k(= 0.5)$ is the model constant. The rationale of the model functions and constants in Eqs. (9)–(12) is discussed in detail in Inagaki[15].

The SGS filter width Δ is defined as

$$\Delta = \sqrt{\text{the maximum area among the faces of a cell}}\ . \tag{13}$$

In the Cartesian structured grid system, the above definition can be rewritten as

$$\Delta = \sqrt{\max\left(\Delta_x\Delta_y, \Delta_y\Delta_z, \Delta_z\Delta_x\right)}\ . \tag{14}$$

This definition is the same as that given in the hybrid LES/RANS model of Abe[16]. The advantage of the present definition is that it can exclude the effect of the grid width in the wall-normal direction, which is generally much smaller than that in other directions near the wall. Note that by using Eq. (13), we can reasonably determine Δ even in a non-orthogonal or an unstructured grid system.

Table 1 Computational parameters for channel-flow cases.

Case	Re_τ	Domain	Grid nodes
C395F	395	$6\delta \times 2\delta \times 1.5\delta$	$61 \times 61 \times 61$
C395C	395	$12\delta \times 2\delta \times 3\delta$	$31 \times 61 \times 31$
C1E3	1020	$6\delta \times 2\delta \times 1.5\delta$	$121 \times 101 \times 31$
C5E3	5000	$6\delta \times 2\delta \times 1.5\delta$	$201 \times 111 \times 51$

Case	Δx^+	Δy^+	Δz^+	Δt
C395F	40	0.8 – 36	10	1×10^{-3}
C395C	160	0.8 – 36	40	1×10^{-3}
C1E3	51	1.0 – 51	51	5×10^{-4}
C5E3	150	1.0 – 150	150	2×10^{-4}

3 Test Cases and Computational Conditions

First, to validate the basic predictive performance, the present SGS model was applied to fundamental plane channel flows. In this study, three Reynolds-number cases were tested, namely $Re_\tau = 395, 1020$ and 5000, where the Reynolds number was based on the friction velocity u_τ and the half channel height δ. The computational conditions are summarized in Table 1. The grid resolution of C395F ($Re_\tau = 395$) is thought to be sufficient for reasonable LES, while C395C is approximately the grid resolution at which the prediction accuracy of the LES begins to clearly decrease. The results obtained for these cases at $Re_\tau = 395$ are compared with corresponding DNS data[17]. In contrast, C1E3 and C5E3 were adopted to confirm the applicability of the present SGS model to higher-Re turbulence. Furthermore, the SGS components predicted in C395F were investigated in detail to obtain valuable knowledge for further development of this type of SGS modeling.

Next, to investigate the model performance for complex turbulence with flow impingement, the present SGS model was applied to a plane impinging jet. In this case, the computational conditions given in Table 2 were taken from the DNS of Hattori and Nagano[18]. Figure 1 is a schematic illustration of this case, where D is the inlet channel width. In this study, the grid nodes consisted of $261 \times 61 \times 46$ covering a domain of $40D(-20D \leftrightarrow 20D) \times 2D \times 1.5D$ in the x-, y- and z-directions, respectively. According to the DNS, driver-channel flow was simultaneously calculated for the inlet condition. In the calculation, the Reynolds number for the driver channel flow was fixed based on the mean friction velocity and the inlet channel width. The bulk Reynolds number finally obtained was about 9000 (based on the inlet bulk-mean velocity U_b and the hydraulic diameter $2D$), which was close to that of the DNS[18].

Finally, to confirm the usefulness of the present SGS model for complex turbulence with flow separation, the model was applied to 3-D diffuser flow. This test case was studied at the ERCOFTAC Workshop[19] on Refined Turbulence Modeling for further development of turbulence models currently used. For this test case, the corresponding experiment was carried out by Cherry et al.[20] and detailed data were provided for comparison. Figure 2 is a schematic illustration of this case. This experimental facility had a long duct with a constant rectangular cross-

Table 2 Computational parameters of the plane impinging jet.

Case	Re	Domain	Grid nodes
PIJ	9000	$40D$ $(-20D \leftrightarrow 20D)\times 2D\times 1.5D$	$261 \times 61 \times 46$

Case	$\Delta x/D$	$\Delta y/D$	$\Delta z/D$	Δt
PIJ	0.0015 – 0.35	0.0015 – 0.08	0.033	5×10^{-4}

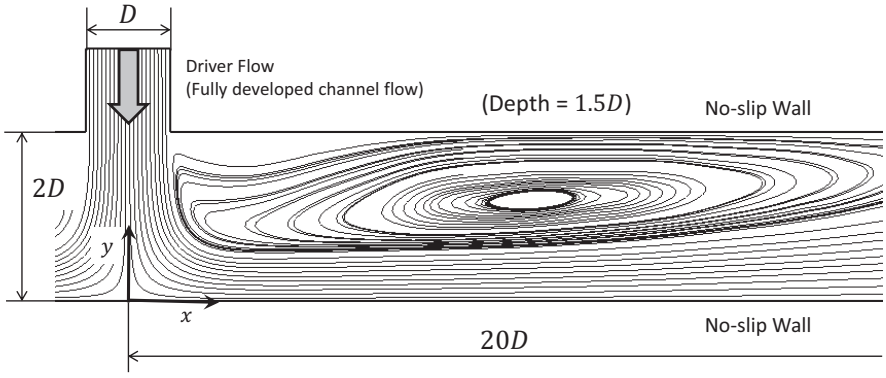

Fig. 1 Schematic view and representative streamlines of the plane impinging jet.

section of 1cm height (H) and 3.33cm width (W), resulting in a fully-developed turbulent flow at the end of the rectangular duct. The Reynolds number in the experiment was 10,000 based on the height and bulk-mean velocity of the inlet duct. The rectangular duct was connected with a 15cm long asymmetric diffuser that had a 4cm square-duct outlet section. The flow had highly three-dimensional separation in the diffuser region, which showed considerable sensitivity to the characteristics of the diffuser geometry. In this sense, the application is appropriate to investigate in detail the model performance. An important concern may be the prediction accuracy of the present SGS model for such a complex turbulent flow with various grid resolutions. To examine this issue, three grid resolutions were tested for the 3-D diffuser flow, as summarized in Table 3. Similar to the impinging-jet case, driver-duct flow was simultaneously calculated for the inlet condition. The Reynolds number for the driver duct flow was fixed based on the mean friction velocity and inlet duct height. As seen in Table 3, the bulk Reynolds number finally obtained in each case was sufficiently close to that observed in the experiment.

Calculations were performed using an unstructured finite-volume procedure that was almost the same as that used by Muto et al.[21], where vertex-centered type of storage was used on the grid. The second-order central difference scheme was used to discretize the spatial derivatives except for the convection term of k_{SGS} (Eq. (12)), which was discretized using the second-order upwind scheme. Note that structured grids were used in the present simulations, and the predictive

Table 3 Computational parameters for 3-D diffuser-flow cases.

Case	Diffuser nodes	$\Delta x/H$	$\Delta y/H$	$\Delta z/H$	Re
D1F	$312 \times 67 \times 121$	0.06 – 0.3	0.003 – 0.1	0.003 – 0.05	9300
D1M	$251 \times 51 \times 91$	0.08 – 0.3	0.003 – 0.13	0.003 – 0.06	9500
D1C	$200 \times 41 \times 71$	0.12 – 0.3	0.005 – 0.17	0.005 – 0.09	9600

Case	Driver nodes	$\Delta x/H$	$\Delta y_{max}/H$	$\Delta z/H$	Δt
D1F	$81 \times 67 \times 121$	0.06	0.02	0.03	1×10^{-3}
D1M	$67 \times 51 \times 91$	0.08	0.03	0.05	1×10^{-3}
D1C	$46 \times 41 \times 71$	0.12	0.04	0.07	1×10^{-3}

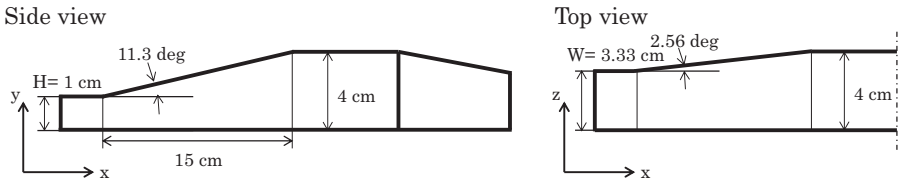

Fig. 2 Schematic view of 3-D diffuser flow.

performance was thus equivalent to that of a collocated structured grid system with the same level of discretization scheme being adopted.

The time marching was based on the fractional step method[22], in which the second-order Crank-Nicolson scheme was used for the velocity equations. On the other hand, for the transport equation of k_{SGS}, the first-order Euler implicit scheme was used. The coupling of the velocity and pressure fields was based on the SMAC (simplified marker and cell) method[23]. The flow rate on the control-volume surface was estimated using Rhie–Chow interpolation[24]. Since a first-order time-marching scheme and a second-order upwind scheme were adopted for the k_{SGS} transport equation, we conducted an additional simulation for the plane impinging-jet case to confirm the effects of the schemes on the predictive performance. In the calculation, the time step was reduced by half and the second-order central difference scheme was adopted for the convection term of the k_{SGS} transport equation. The obtained results are summarized in the Appendix. From the comparison of the simulation results given below with those in the Appendix, we see that the time-integration and space-discretization schemes do not have any crucial effect on the present computational results.

For the boundary conditions, a periodic condition was imposed in the streamwise and spanwise directions for the channel-flow cases. A periodic condition was also used in the spanwise direction of the plane impinging jet. For the driver section of the plane impinging jet and the 3-D diffuser flow, a periodic boundary condition was specified in the streamwise direction and the obtained unsteady flow field was then imposed at the inlet of the main computational domain at each time step. At the outlet boundaries of the plane impinging jet and the 3-D diffuser flow, zero streamwise gradients were prescribed. On the other hand, at the wall surfaces in all test cases, no-slip conditions were specified.

To explore the model performance in detail, we performed some additional computations with other conventional SGS models; i.e., the Smagorinsky model and dynamic Smagorinsky model. Concerning the computations with the Smagorinsky model, a general Van Driest damping function was used in the near-wall region. On the other hand, as for the computation with the dynamic Smagorinsky model, a conventional linear EVM expression was used[2][3]. Note that since such a dynamic SGS model generally has strong numerical instability, we introduced a well-known strategy of clipping the negative values of ν_{SGS} to realize stable computation.

4 Results and Discussion

4.1 Channel flow

First, the computational results for the channel-flow cases are analyzed. Representative results for C395F (i.e, the mean velocity, the turbulence intensities and the Reynolds shear stress) are compared with the corresponding DNS data[17] in Fig. 3. The comparison shows good agreement because the grid resolution used was reasonably fine. Figure 4 compares the distributions of the mean velocity predicted by the Smagorinsky model, the original isotropic SGS model and the present anisotropic SGS model, respectively. Note that the original isotropic SGS model is composed of only the first and second terms on the right-hand side of Eq. (7). This is the standard EVM-type linear form that has been used most often. As seen in Fig. 4 (a) and (b), the prediction accuracy of the EVM-type linear SGS models becomes worse as the grid resolution becomes coarser. However, Fig. 4 (c) shows that the present anisotropic SGS model returns reasonable predictions for both grid-resolution cases. From the comparison of Fig. 4 (b) and (c), it is seen that the extra anisotropic term in Eq. (7) is essential for improving the predictive performance. Figure 5 compares the mean-velocity distributions for the higher-Re cases (C1E3 and C5E3) predicted by the Smagorinsky model and the present SGS model. Although the grid resolutions used in these cases are thought to be too coarse for LES, it is found that the prediction accuracy is considerably improved by introducing the present anisotropy-resolving SGS modeling concept.

Figure 6 compares the distributions of the second invariant of the velocity-fluctuation gradient tensor obtained with the original isotropic and the present anisotropic SGS models for C395C. In the figure, only the region from the lower wall to the channel center is visualized, and the color shows the distance from the lower wall. Different trends for the original and present models are seen. Considering that the blue region very close to the wall surface disappears in Fig. 6 (a), the near-wall eddy structures definitely decrease in the results obtained with the original model. When a conventional LES is applied to a coarse grid resolution, small-size near-wall eddy structures can no longer be resolved. In contrast, the blue region indicating the near-wall eddy structures remain in Fig. 6 (b) with the introduction of the extra anisotropic term. This is thought to lead to more reasonable predictions of the mean velocity using the present SGS model.

Since the prediction accuracy for C395F is sufficient, the LES data obtained here are thought to be useful for detailed discussion on fundamental features of the present SGS modeling concept. Figure 7 compares the distributions of the time-averaged GS and SGS stress components. Although the SGS stresses are

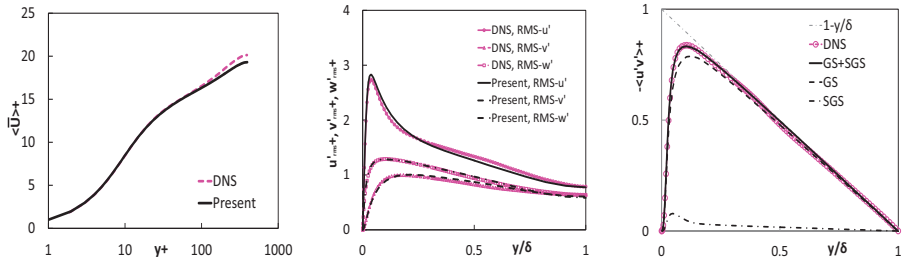

(a) Mean velocity (b) Turbulence intensities (c) Reynolds shear stress

Fig. 3 Computational results of channel flow for C395F.

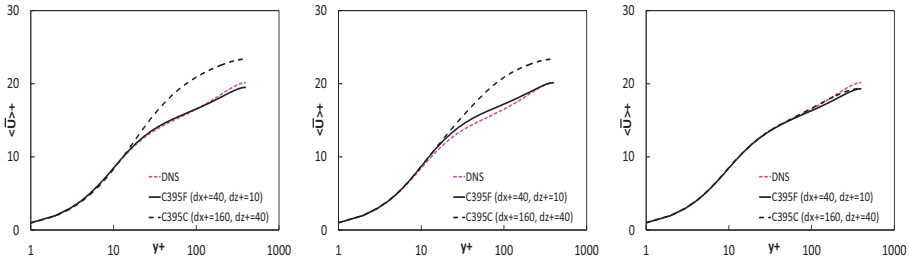

(a) Smagorinsky model (b) Original Isotropic model (c) Present model

Fig. 4 Comparison of mean-velocity distributions with results obtained with other models at $Re_\tau = 395$.

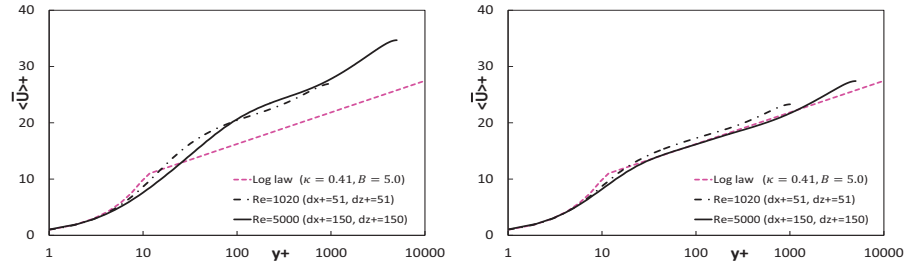

(a) Smagorinsky model (b) Present model

Fig. 5 Comparison of mean-velocity profiles of higher-Re channel flows (C1E3 and C5E3).

much smaller than the GS stresses, strong stress anisotropy is clearly seen in their distributions. In Fig. 7 (c), the distributions of the SGS anisotropy tensor, $b_{ij} = \tau_{ij}/2k_{SGS} - \delta_{ij}/3$, are compared with those of the GS components. It is interesting that the GS and SGS stresses have similar trends in terms of the stress anisotropy, although detailed inspection indicates a slightly more isotropic feature in the SGS stress components.

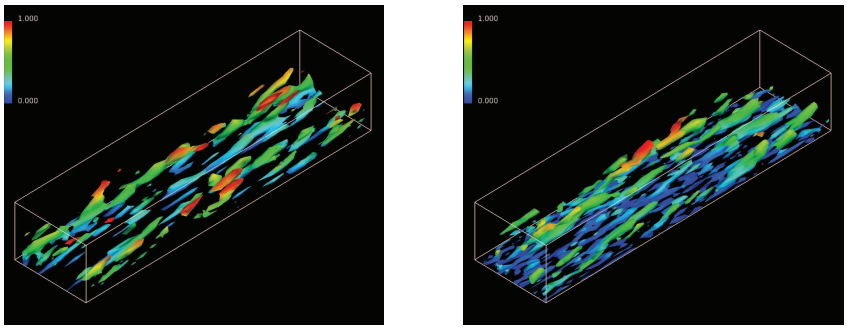

(a) Original isotropic model (b) Present anisotropic model

Fig. 6 Second invariant of the velocity-fluctuation gradient tensor for C395C (color: wall distance).

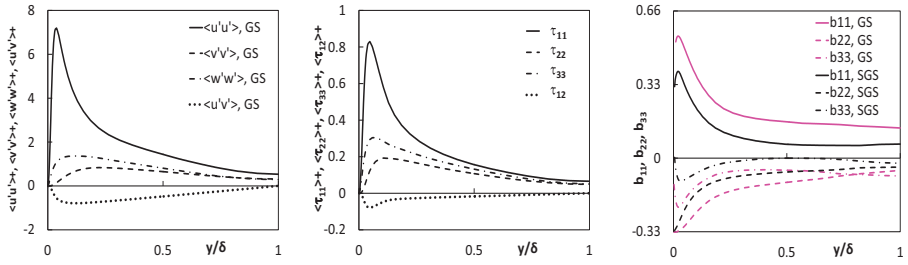

(a) GS stresses (b) SGS stresses (c) Anisotropy tensor

Fig. 7 Comparison of GS and SGS stresses in the channel-flow case.

Another important concern is the contribution of each term in Eq. (7) to the stress anisotropy. To discuss this issue, Fig. 8 compares the distributions of the time-averaged SGS stresses calculated with the linear EVM term ($-2\nu_{SGS}S_{ij}$) and the extra term ($2k_{SGS}b_{ij}^{SGS}$). Figure 8 (a) shows that the linear EVM term mainly contributes to the SGS shear stress, although it returns very small values of the SGS normal stresses as shown in Fig. 8 (b). It is thus said that the linear EVM term does not contribute to the stress-anisotropy prediction. In contrast, Fig. 8 (c) clearly shows that the extra anisotropic term is dominant in predicting the SGS stress anisotropy. It should be noted again that R_{ij}^{*} in Eq. (6) yields no undesirable energy transfer between the GS and SGS components that may cause computational instability, although the SGS normal stresses calculated by the extra term are much larger than those calculated by the linear EVM term. Although the values calculated with the linear EVM term are very small, as seen in Fig. 8 (b), they control the energy transfer in this case.

Figure 9 compares the anisotropy tensor predicted using the present SGS model with that predicted using the original Bardina model. Note that the SGS components of the original Bardina model were evaluated in an *a priori* test using the simulation results of the present SGS model. In this calculation, $C_B = 2$ was

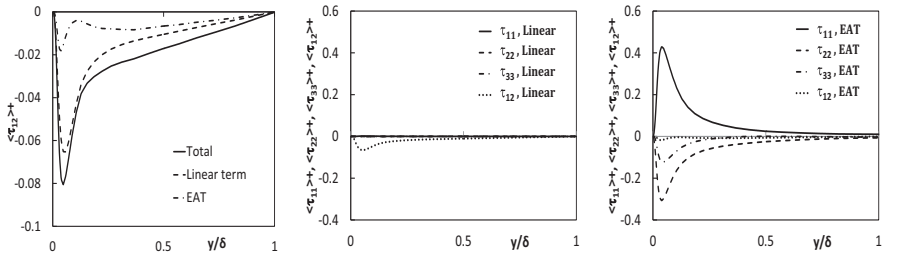

(a) SGS shear stress (b) Linear EVM term (c) Extra anisotropic term

Fig. 8 Comparison of linear and anisotropic terms in the channel-flow case.

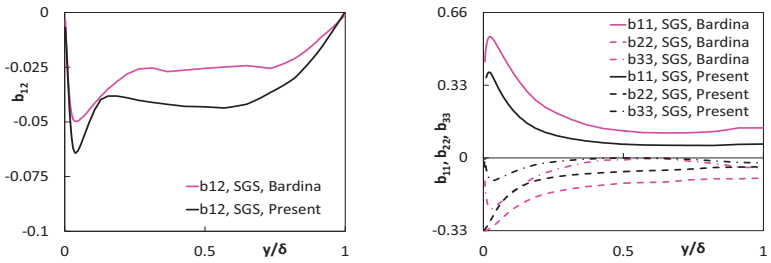

(a) SGS-shear stress (b) SGS-normal stresses

Fig. 9 Distributions of the anisotropy tensor in an *a priori* test of the original Bardina model in the channel-flow case.

adopted in accordance with the study by Inagaki et al.[25]. However, the main concern of Fig. 9 is to investigate the SGS stress anisotropy by comparing the anisotropy-tensor components. As found in the definition, the anisotropy tensor of the Bardina model does not depend on the model constant CB because it appears in both numerator and denominator. Therefore, at least in this study, the value of the model constant CB has no effect on the discussion. As seen in the figure, the results of the original Bardina model are similar to those of the present SGS model, although there are small differences between the results. This indicates that the present extra anisotropic term reflects the fundamental features of the original Bardina model.

4.2 Plane impinging jet

The distributions of the streamwise mean velocity are shown in Fig. 10. Note that the predictions made with the Smagorinsky model are also included for comparison. The present results generally correspond well to the DNS data[18], although detailed comparison reveals slight discrepancies particularly in the upper-wall region. On the other hand, it is seen that the results by the Smagorinsky model also show similar predictions. This may originate from a considerably low Reynolds number condition for this test case. Considering this fact, at least now, it can

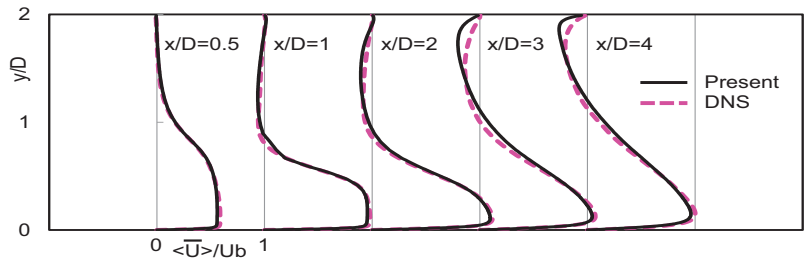

(a) The present model

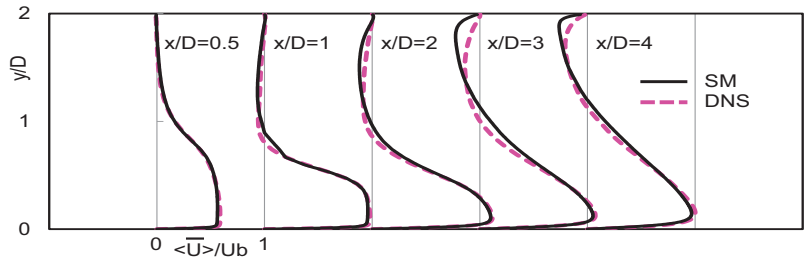

(b) Smagorinsky model

Fig. 10 Computational results of streamwise mean velocity for the plane impinging jet.

be said that the present SGS model generally works well with the computational stability being maintained even for complex turbulence, as well as in channel-flow cases.

Figure 11 compares the computational results of the mean velocity and the turbulence intensities predicted by the present SGS model with the DNS data at $x/D = 0$ and $x/D = 4$. It is found that the flow phenomena are considerably different between the stagnation region ($x/D = 0$) and the wall-jet region ($x/D = 4$). Although there are some discrepancies in the results of the turbulence intensities, the fundamental features of this type of flow field are well captured by the present simulation. Considering that far fewer grid nodes were used in this simulation than in DNS, the present simulation results are thought to be generally acceptable. It is thus considered that the present LES data can be used to investigate in detail the characteristics of the present SGS modeling concept for complex turbulence with flow impingement, although the deficiencies presently seen are expected to be overcome in future studies.

Figure 12 compares the time-averaged GS and SGS stress components in the stagnation region at $x/D = 0$. It is clearly seen that the trends of the GS stress components are completely different from those in the channel-flow case. As seen in Fig. 12 (b), the SGS stresses also have trends different from those in the channel-flow case (see Fig. 7 (b)), with the trends being rather similar to those of the GS stresses in the stagnation region of the impinging jet. This is also confirmed by the comparison of the stress anisotropy (as shown in Fig. 12 (c)), where the spanwise (z-) component has a maximum value in the vicinity of the wall for both the GS and SGS stresses, while the stress component in the x-direction is small everywhere except the region very close to the wall surface.

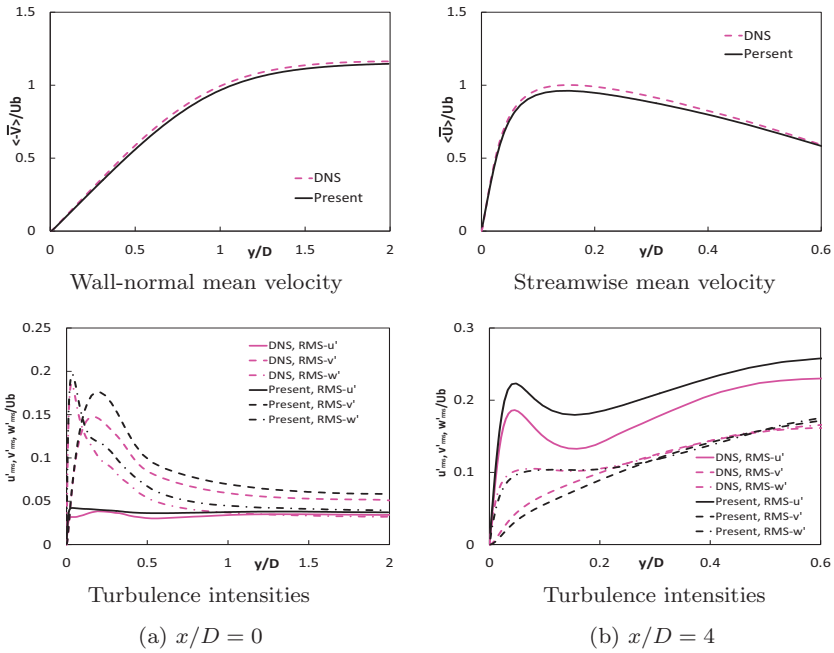

(a) $x/D = 0$ (b) $x/D = 4$

Fig. 11 Comparison of the results with DNS data for the plane impinging jet.

On the other hand, Fig. 13 compares the time-averaged GS and SGS stress components at $x/D = 4$. As shown in Fig. 10, in this region, a wall jet is developing on the lower wall in the x-direction. Figure 13 (a) indicates that the GS stresses have trends rather similar to those in wall-shear flow, in which the streamwise stress component is largest in the near-wall region. It is found from Fig. 13 (b) that the characteristics of the SGS stresses are qualitatively similar to those of the GS stresses. This is endorsed by comparison of the stress anisotropy between the GS and SGS stresses as seen in Fig. 13 (c). Although there are some discrepancies, the fundamental features are very similar.

4.3 3-D diffuser flow

From the aforementioned discussion, the present SGS model is expected to work properly not only for fundamental wall-shear flows but also for more complex turbulence. Therefore, to validate the model performance for other representative complex turbulence (e.g., a flow field with massive separation), the computational results of 3-D diffuser flow are investigated.

Figure 14 shows the mean friction coefficient for the driver duct flow. In the figure, the predictions made with the Smagorinsky model and dynamic Smagorinsky model are included for comparison. Note that in the case of the Smagorinsky model, calculations of the driver duct were also made for D1F and D1M. It is found that the grid dependency of the present SGS model is sufficiently weak for the variation in the grid resolution. In contrast, the Smagorinsky model has

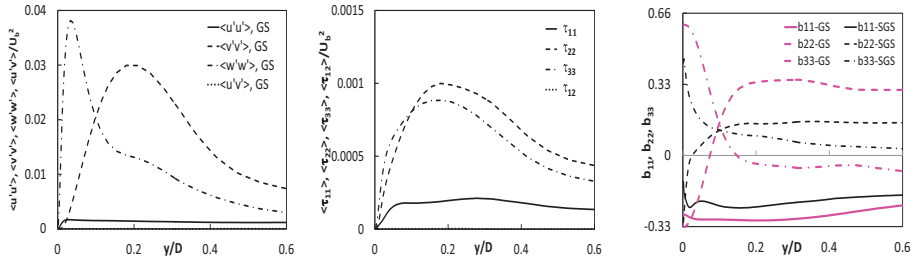

(a) GS stresses (b) SGS stresses (c) Anisotropy tensor

Fig. 12 Comparison of GS and SGS stresses for the plane impinging jet ($x/D = 0$).

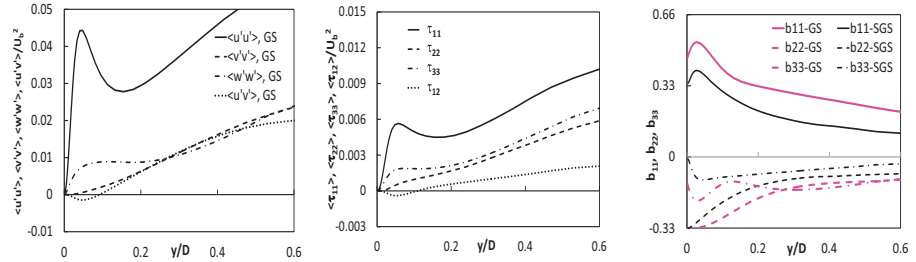

(a) GS stresses (b) SGS stresses (c) Anisotropy tensor

Fig. 13 Comparison of GS and SGS stresses for the plane impinging jet ($x/D = 4$).

much larger grid dependency. It is also seen that the dynamic Smagorinsky model returns a value similar to the Smagorinsky model for D1C. Considering that the dynamic Smagorinsky model had strong grid dependency in our previous study[11], it is thought that this model will have a trend similar to that of the Smagorinsky model. These features are thought to be important from an engineering viewpoint.

The predictions made with the present SGS model are compared with experimental data[20] in Figs. 15–19. Figure 15 shows the predicted pressure coefficients at the center plane ($z/W = 1/2$) on the lower wall. The computational results are in good agreement with the experimental data for all test cases. It should be noted again that the grid dependency of the results is weak for the variation in the grid resolution.

Figure 16 shows contour distributions of the streamwise velocity at representative cross-stream sections. On the other hand, Fig. 17 compares the predicted zero-streamwise velocity contours with the experimental data. In Fig. 17, comparison is carried out in two spanwise sections; i.e., the center plane ($z/W = 1/2$) and a plane close to the side wall ($z/W = 7/8$). A massive separation is clearly seen in the region along the upper wall, and the flow reattaches in the downstream straight-duct region. The predictions generally correspond well to the experimental data. In particular, it is worth noting that reasonable results are obtained even for the coarse grid-resolution case of D1C, although the predicted separation bubble is slightly smaller than the observed bubble in the other cases.

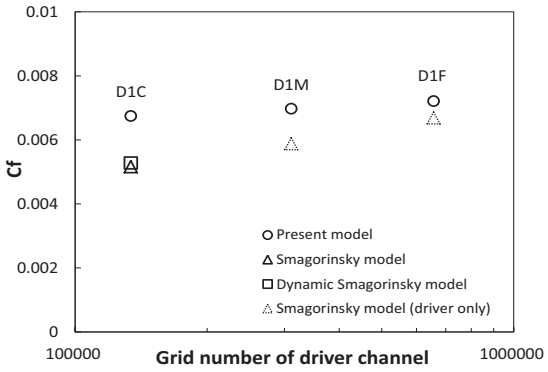

Fig. 14 Comparison of mean-friction coefficients in the driver duct part of 3-D diffuser flow.

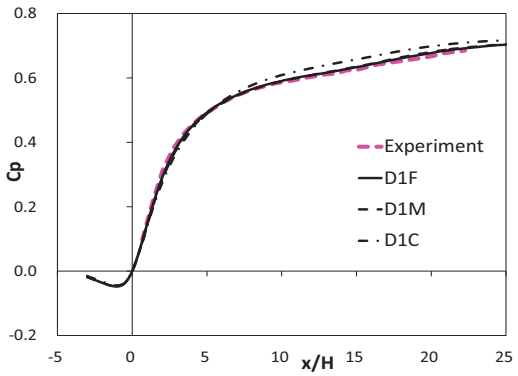

Fig. 15 Comparison of center-plane pressure coefficients for the lower wall in 3-D diffuser flow.

The profiles of the mean velocity and the streamwise turbulence intensity across the two aforementioned spanwise sections (i.e., $z/W = 1/2$ and $z/W = 7/8$) are compared in Figs. 18 and 19, respectively. The figures show that the predictions are generally in good agreement with the experimental data for all grid resolutions. Although there are still discrepancies, the present SGS model generally returns reasonable predictions not only in the center region but also in the side-wall region. Therefore, the predicted three-dimensional flow pattern generally corresponds well to that of the experiment. It also indicates the applicability of the present SGS model to complex turbulence with massive flow separation.

Finally, representative results for D1C obtained with the Smagorinsky model and dynamic Smagorinsky model are shown in Figs. 20 and 21. It is a little surprising that the results normalized by the inlet mean velocity look reasonable, although the mean friction coefficients predicted by these models are thought to be unreasonable, as discussed in Fig. 14. This fact may be largely because of a considerably low Reynolds number condition adopted in this study, as well as the impinging-jet case. However, as found in the channel-flow cases, the Smagorinsky

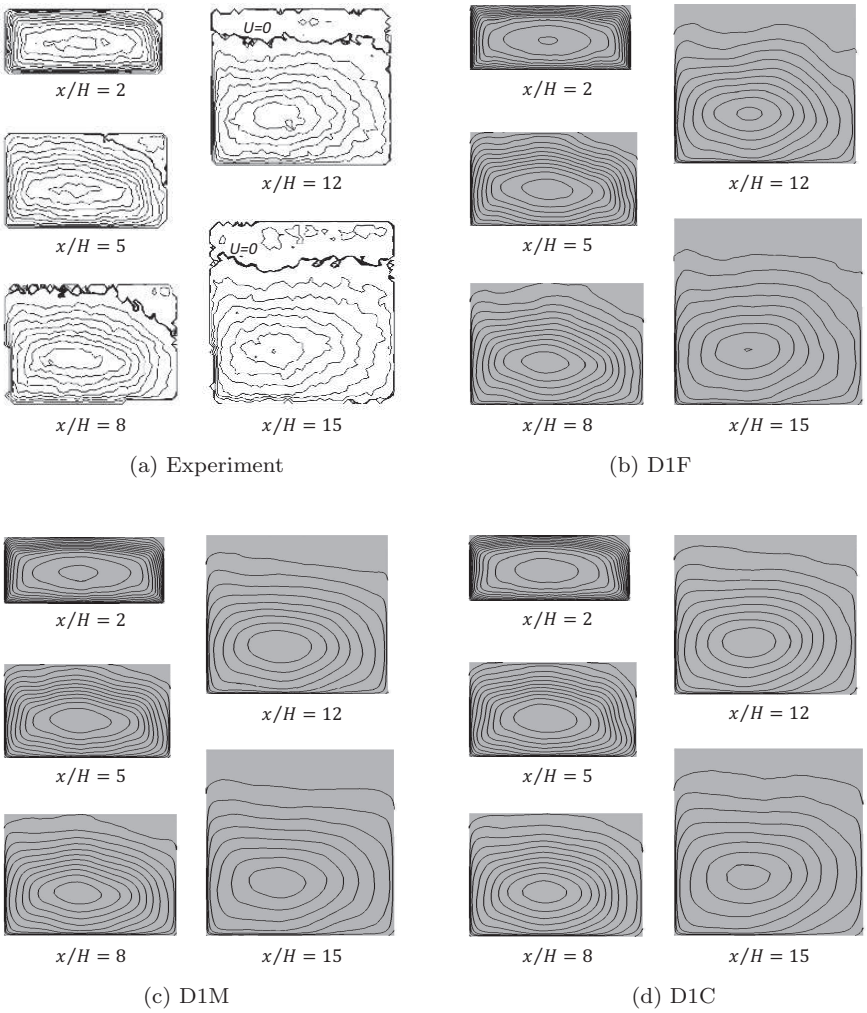

Fig. 16 Contour distributions of streamwise velocity at various cross-stream sections.

model could not give reasonable predictions with very coarse-grid resolutions. It has been reported by Abe[11] that the dynamic Smagorinsky model is likely to show a similar trend. This is also seen in Fig. 5 under high-Re conditions. Therefore, the present SGS model is expected to show its potential when it is applied to higher-Re complex turbulence.

5 Concluding Remarks

An anisotropy-resolving SGS model for large eddy simulation was investigated. This SGS model is constructed by combining an isotropic linear eddy-viscosity

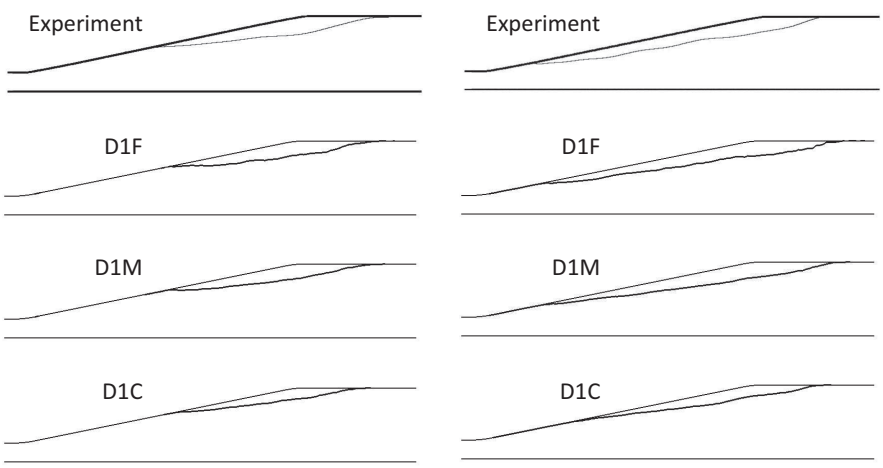

(a) $x/W = 1/2$ (b) $x/W = 7/8$

Fig. 17 Comparison of zero-streamwise velocity contours of 3-D diffuser flow.

model with an extra anisotropic term. Since the extra anisotropic term is modeled to prevent undesirable energy transfer between GS and SGS parts, the model is expected not to seriously affect the computational stability. To validate the predictive performance of this SGS model for complex turbulence with flow impingement and/or flow separation, the model was applied to numerical simulations of a plane impinging jet and 3-D diffuser flow as well as fundamental plane channel flows. This anisotropy-resolving SGS model provided reasonable predictions for these test cases. Although the present model gives highly anisotropic SGS stress components, all the calculations were stably performed. This feature means that the present SGS model can improve the predictive performance without seriously affecting the computational stability. Through the above discussion, the present study revealed the usefulness of the present anisotropy-resolving SGS modeling in practical engineering applications, although there remain several issues to be investigated. Among them, the next important concern to address may be a detailed assessment of the model performance for higher-Re complex turbulence.

Acknowledgements This research was supported by Grant-in-Aid for Scientific Research 24560197, sponsored by the Japan Society for the Promotion of Science. Support was also provided by the "Advanced Computational Scientific Program" of the Research Institute for Information Technology, Kyushu University, Japan. Computations were mainly carried out using computer facilities at the Research Institute for Information Technology, Kyushu University, Japan.

Appendix

To confirm the effect of the time-integration and space-discretization methods used in the k_{SGS} transport equation on the predictive performance, we conducted an additional simulation for the plane impinging jet, where the time step was reduced

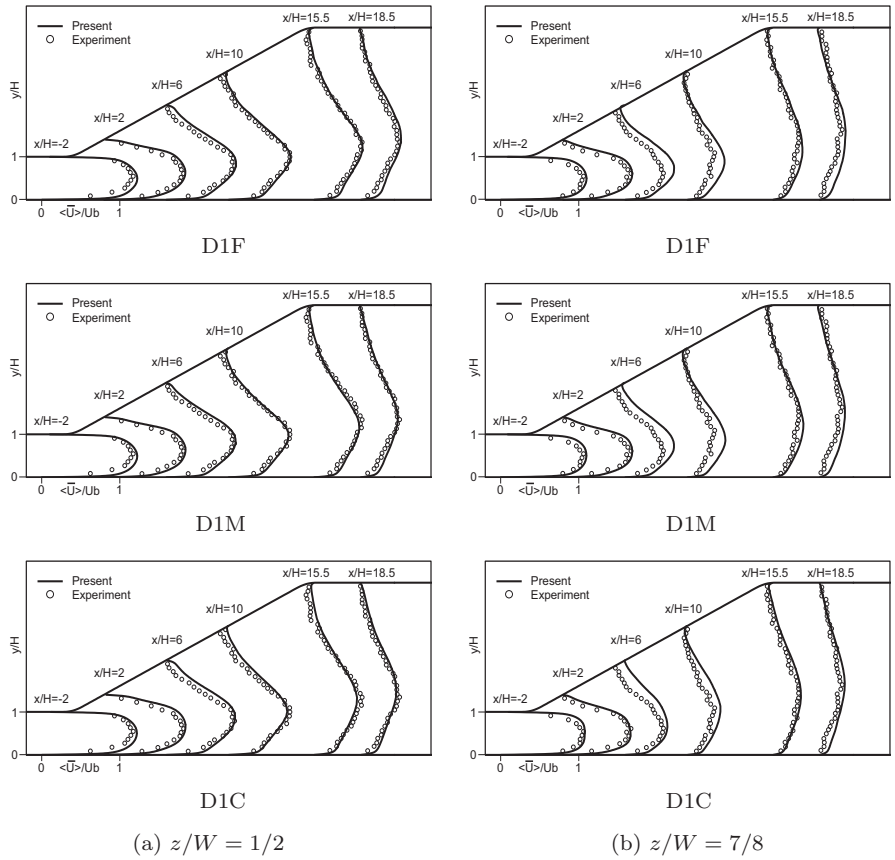

(a) $z/W = 1/2$ (b) $z/W = 7/8$

Fig. 18 Comparison of mean-velocity profiles with experimental data for 3-D diffuser flow.

by half and the second-order central difference scheme was adopted for the convection term of the k_{SGS} transport equation. The mean-velocity predictions made with the present anisotropic SGS model are shown in Fig. 22. The fundamental features of the predictions are very similar to those shown in Fig. 10. Next, Fig. 23 shows the predictions of the turbulent statistics across two streamwise cross sections. We see that the distributions of these turbulent statistics correspond well to those shown in Fig. 11. Although a close inspection may indicate that some discrepancies remain in the turbulence-intensity distributions, it is understood from these comparisons that the schemes adopted in this study have no crucial negative effects on the simulation results.

References

1. J. Smagorinsky, General circulation experiments with the primitive equations: I. The basic experiment, *Mon. Weather Rev.*, **91**, 99-164 (1963).
2. M. Germano, U. Piomelli, P. Moin and W.H. Cabot, A dynamic subgrid-scale eddy viscosity model, *Phys. Fluids A*, **3**, 1760-1765 (1991).

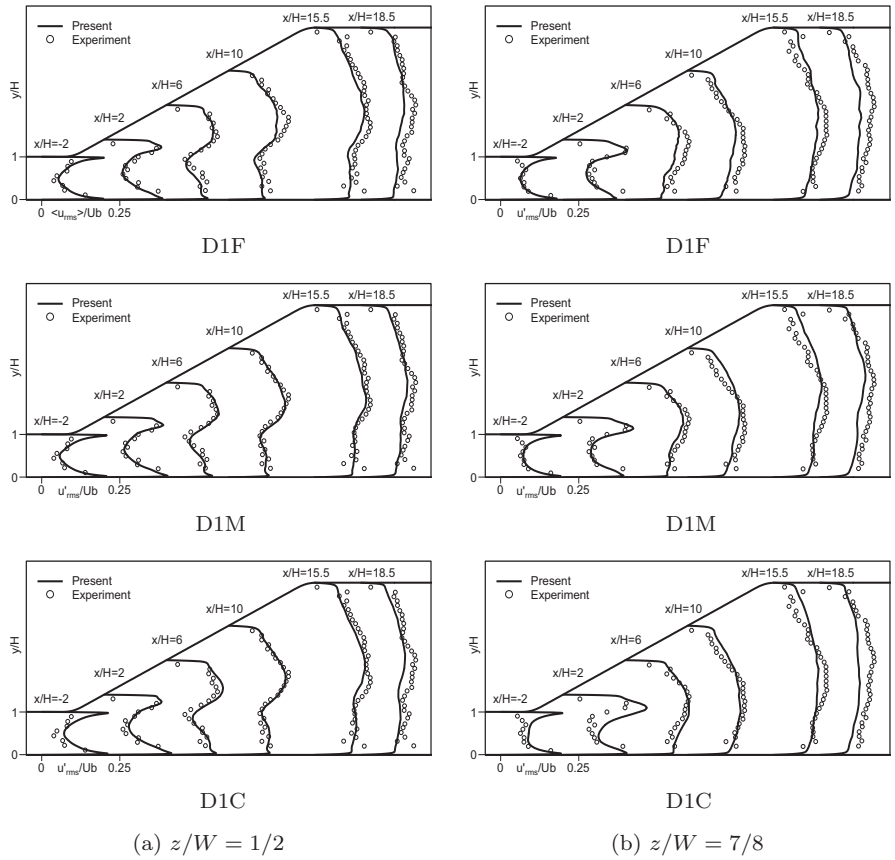

(a) $z/W = 1/2$ (b) $z/W = 7/8$

Fig. 19 Comparison of streamwise turbulence-intensity profiles with experimental data for 3-D diffuser flow.

3. D.K. Lilly, A proposed modification of the Germano subgridscale closure method. *Phys. Fluids A*, **4**, 633-635 (1992).
4. J. Bardina, J.H. Ferziger and W.C. Reynolds, Improved subgrid scale models for large eddy simulation, *AIAA Paper*, 80-1357 (1980).
5. K. Horiuti, A proper velocity scale for modeling subgrid-scale eddy viscosities in large eddy simulation, *Phys. Fluids A*, **5**, 146-157 (1993).
6. Y. Zang, R.L. Street and J.R. Koseff, A dynamic mixed subgrid-scale model and its application to turbulent recirculating flows, *Phys. Fluids A*, **5**, 3186-3196 (1993).
7. B. Vreman, B. Geurts and H. Kuerten, On the formulation of the dynamic mixed subgrid-scale model, *Phys. Fluids*, **6**, 4057-4059 (1994).
8. K. Horiuti, A new dynamic two-parameter mixed model for large-eddy simulation, *Phys. Fluids*, **9**, 3443-3464 (1997).
9. F. Sarghini, U. Piomelli and E. Balaras, Scale-similar models for large-eddy simulations, *Phys. Fluids*, **11**, 1596-1607 (1999).
10. Y. Morinishi and O.V. Vasilyev, A recommended modification to the dynamic two-parameter mixed subgrid scale model for large eddy simulation of wall bounded turbulent flow, *Phys. Fluids*, **13**, 3400-3410 (2001).
11. K. Abe, An improved anisotropy-resolving subgrid-scale model with the aid of a scale-similarity modeling concept, *Int. J. Heat Fluid Flow*, **39**, 42-52 (2013).

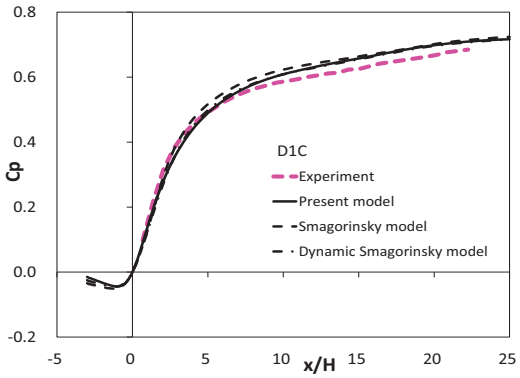

Fig. 20 Comparison of center-plane pressure-coefficient profiles for the lower wall with the results obtained with other models in the case of D1C.

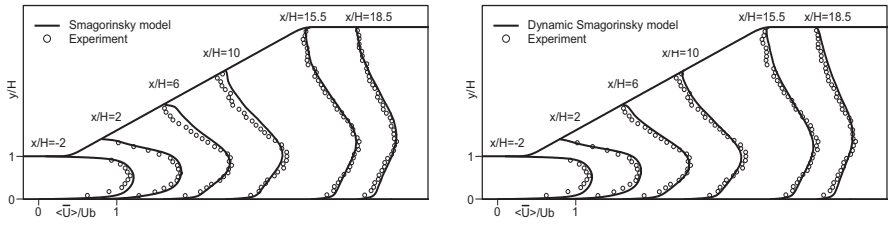

(a) Smagorinsky model (b) Dynamic Smagorinsky model

Fig. 21 Comparison of mean-velocity profiles at $z/W = 1/2$ in the case of D1C.

12. T.B. Gatski and C.G. Speziale, On explicit algebraic stress models for complex turbulent flows. *J. Fluid Mech.*, **254**, 59-78 (1993).
13. T.B. Craft, B.E. Launder and K. Suga, Prediction of turbulent transitional phenomena with a nonlinear eddy viscosity model. *Int. J. Heat Fluid Flow*, **18**, 15-28 (1997).
14. K. Abe, T. Kondoh and Y. Nagano, Y. On Reynolds stress expressions and near-wall scaling parameters for predicting wall and homogeneous turbulent shear flows. *Int. J. Heat Fluid Flow*, **18**, 266-282 (1997).
15. M. Inagaki, A new wall-damping function for large eddy simulation employing Kolmogorov velocity scale, *Int. J. Heat Fluid Flow*, **32**, 26-40 (2011).
16. K. Abe, A hybrid LES/RANS approach using an anisotropy-resolving algebraic turbulence model, *Int. J. Heat Fluid Flow*, **26**, 204-222 (2005).
17. R.D. Moser, J. Kim and N.N. Mansour, Direct numerical simulation of turbulent channel flow up to Re_τ=590, *Phys. Fluids*, **11**, 943-945 (1999).
18. H. Hattori and Y. Nagano, Direct numerical simulation of turbulent heat transfer in plane impinging jet, *Int. J. Heat Fluid Flow*, **25**, 749-758, (2004).
19. ERCOFTAC Workshop (edited by S. Jakirlic, G. Kadavelil, E. Sirbubalo and D. Borello), *Proc. 14th SIG15 ERCOFTAC Workshop on Refined Turbulence Modelling, Case 13.2: Flow in a 3-D diffuser*, Rome, http://130.83.243.201/ercoftac14/workshop2009.html, (2009).
20. E.M. Cherry, C.J. Elkins and J.K. Eaton, Geometric sensitivity of three-dimensional separated flows, *Int. J. Heat Fluid Flow*, **29**, 803-811 (2008).
21. M. Muto, M. Tsubokura and N. Oshima, Negative Magnus lift on a rotating sphere at around the critical Reynolds number, *Phys. Fluids*, **24**, 014102 (2012).
22. J. Kim and P. Moin, Application of a fractional-step method to incompressible Navier-Stokes equations. *J. Comput. Phys.*, **59**, 308-323 (1985).

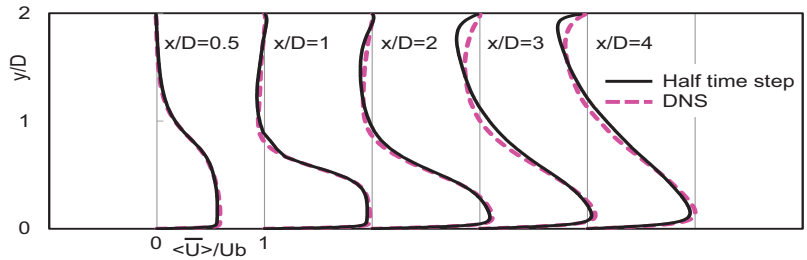

Fig. 22 Streamwise mean-velocity distributions of the plane impinging jet. (The time step was reduced by half and the second-order central difference was used for convection in the k_{SGS} equation.)

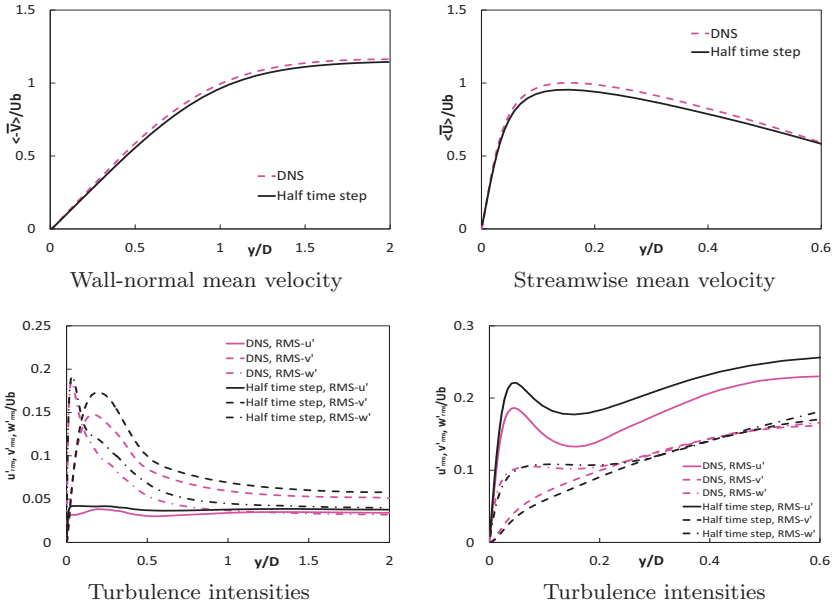

Wall-normal mean velocity | Streamwise mean velocity

Turbulence intensities | Turbulence intensities

(a) $x/D = 0$ (b) $x/D = 4$

Fig. 23 Comparison of the results with DNS data for the plane impinging jet. (The time step was reduced by half and the second-order central difference was used for convection in the k_{SGS} equation.)

23. A.A. Amsden and F.H. Harlow, A simplified MAC technique for incompressible fluid flow calculations. *J. Comput. Phys.*, **6**, 322-325 (1970).
24. C.M. Rhie and W.L. Chow, Numerical study of the turbulent flow past an airfoil with trailing edge separation. *AIAA J.*, **21**, 1525-1532 (1983).
25. M. Inagaki, T. Kondoh and Y. Nagano, A mixed-time-scale SGS model with fixed model-parameters for practical LES, *J. Fluids Eng.*, **127**, 1-13 (2005).